Nuclear Instruments and Methods in Physics Research A 814 (2016) 82–89

Contents lists available at ScienceDirect

Nuclear Instruments and Methods in Physics Research A

journal homepage: www.elsevier.com/locate/nima

Calculating and optimizing inter-electrode capacitances of charge division microchannel plate detectors

Yan Xing [a,b], Bo Chen [a,*,1], Hong-Ji Zhang [a], Hai-Feng Wang [a], Ling-Ping He [a], Fang-Yuan Jin [a,b]

[a] Changchun Institute of Optics, Fine Mechanics and Physics, Chinese Academy of Sciences, Changchun 130033, China
[b] University of Chinese Academy of Sciences, Beijing 100049, China

ARTICLE INFO

Article history:
Received 30 April 2015
Received in revised form
12 November 2015
Accepted 15 January 2016
Available online 21 January 2016

Keywords:
Charge division micro-channel plate detector
Inter-electrode capacitances
WSZ anode
The finite element method

ABSTRACT

Based on the principle of charge division microchannel plate detectors, the inter-electrode capacitances of charge division anodes which are related to electronic noise of the charge sensitive amplifier and crosstalk effect of the anode are presented. Under all the requirements of charge division microchannel plate detectors such as the imaging linearity and spatial resolution, decreasing the inter-electrode capacitances is one way to improve the imaging performance. In this paper, we illustrate the simulation process of calculating the inter-electrode capacitances. Moreover, a Wedge and Strip (WSZ) anode is fabricated with the picosecond laser micromachining process. Comparing the simulated capacitances and measured capacitances, the three-dimensional finite element method is proved to be valid. Furthermore, by adjusting the design parameters of the anode, the effects of the substrate permittivity, insulation width and the size of pitch on the inter-electrode capacitances have been analysed. The structure of the charge division anode has been optimized based on the simulation data.

1. Introduction

Charge division micro-channel plate detectors, including Vernier anodes and WSZ anodes, are well known for their advantages of linearity, low background noise and high sensitivity [1], making them important tools for observing the earth's plasma sphere. These devices have also been widely used for imaging deep space exploration projects such as IMAGE [2], the J-PEX [3] sounding rocket experiment and the Chang'E-3 project [4]. However, there are still many factors affecting the image resolution of charge division micro-channel plate detectors such as the distribution of the electron cloud [5,6], secondary electron emissions [7,8] and electronic noise of the electronics [9]. One problem that needs to be solved is the crosstalk effect caused by inter-electrode capacitances which directly affect the decoding of charges deposited on charge division anodes. It is well known that although many charge division detectors have different centroid decoding techniques to locate the photon position [10,11], they are mainly based on the principle that signals derived from a single photon are in proportion to the electrode geometry. As a result, the precision of the centroid position is closely related to the charges deposited on the electrodes. The induced charge by inter-electrode capacitances of charge division anodes impairs the image quality. In addition, every inter-electrode capacitance for the signal processing system can be seen as a capacitive load [12–14] adding digital noise to the signal processing system.

Calculating inter-electrode capacitances is essential to achieve better performance and to improve the resolution of the charge division detectors [15]. In this paper, a three-dimensional model has been built according to the charge division microchannel plate detector. For calculation accuracy and convenience, the finite element method has been adopted. Furthermore, the anode characteristics, including the substrate permittivity, width of the insulated channels and the size of pitch, have been discussed by varying the parameters of the anode panel. The finite element method of simulation is a useful tool to considerably reduce the amount of experimental measurements and provides a basis for charge division anode structure design.

2. Charge division microchannel plate detectors system

2.1. Principle of charge division microchannel plate detectors

The overall structure of the detector and primary components are shown in Fig. 1(a) and (b). A single photon from the UV lamp impacts to the MCPs and generates the second electrons to form the charge

* Corresponding author.
E-mail address: chenb@ciomp.ac.cn (B. Chen).
[1] Professor in Changchun Institute of Optics, Fine Mechanics and Physics, mainly engaged in the research of extreme ultraviolet detector and space optics.

http://dx.doi.org/10.1016/j.nima.2016.01.041
0168-9002/

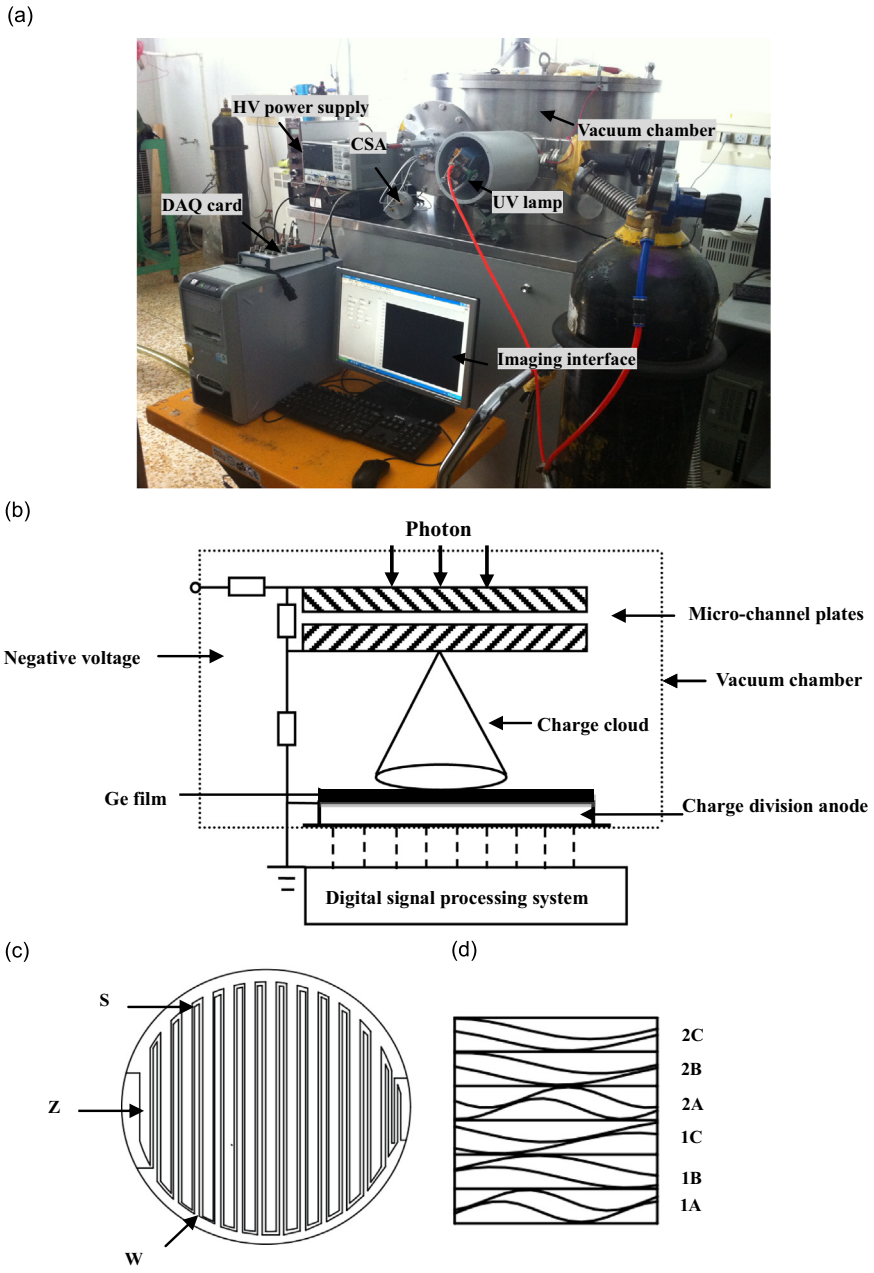

Fig. 1. (a) Structure of charge division micro-channel plate detectors. (b) Motion of a photon in the vacuum chamber. (c) AWSZ anode pattern which consists of strip electrode(S), wedge electrode (W) and Z type electrode (Z). (d) Two pitches Vernier anode pattern taking the form of sine waves, which has three basic units A, B and C.

cloud in the vacuum chamber. The charge cloud is accelerated by the electric field provided by high voltage power and lands on the Ge thin film coated at the back of the anode, which can avoid the second electrons directly contacting with the anode and changing the distribution of charge cloud footprints [16,17]. The charge induced by the Ge film is divided by the anode. Every photon event signal is converted into location information of the charge cloud by a charge sensitive amplifier (CSA), data acquisition card (DAQ) and computer.

A charge division anode is ordinarily manufactured by the picosecond laser processing method to form insulated grooves where electrodes must be arranged side by side on the anode panel, as shown in Fig. 1(c) and (d).

2.2. Electronic noise of the charge sensitive amplifier

The spatial resolution of the charge division anodes is primarily determined by the electronic noise, which is mainly induced by the charge sensitive preamplifier and increases with an increasing input capacitance. The full width at half maximum (FWHM) resolution of the WSZ detectors is determined by [18]

$$dx\ (\mathrm{FWHM}) = \frac{2.35L\left[N^2(1-f)^2+2N^2f^2\right]^{0.5}}{(f_{\max}-f_{\min})Q_{total}}, \tag{1}$$

$$N = N_0 + N_c C_{in}. \tag{2}$$

where L is the anode length, f is the electrode fractional area and f_{max} and f_{min} are the upper and lower limits. Q_{total} is the total charge, N_0 is the preamplifier noise with no capacitive load, N_c is the average electronic noise and C_{in} is the total capacitive load of the amplifier input.

Three charge sensitive amplifiers are independent of each other. Taking the W electrode preamplifier as an example, Fig. 2 is charge sensitive amplifier schematic in which A is the open loop

gain of the integrated amplifier, Q_w is the signal charge of the wedge electrode, C_d are the detector capacitances which mainly correspond to the inter-electrode capacitances of the anode, C_a are the amplifier input capacitances and C_f is the feedback capacitance.

According to the concept of virtual short and virtual open circuit, the voltage and the charge of C_f are

$$U_i - U_0 = U_i - (-A)U_i = (1+A)U_i, \tag{3}$$

$$Q_{c_f} = C_f(U_i - U_0) = C_f(1+A)U_i. \tag{4}$$

It is obtained that

$$C_{in} = C_d + C_a + (1+A)\cdot C_f. \tag{5}$$

From Eq. (4), if the inter-electrode capacitances are calculated, the electronic noise limited spatial resolution of the WSZ detector can be estimated.

2.3. Crosstalk effect of the inter-electrode capacitances on the WSZ anode

Inter-electrode capacitances of the WSZ anode which can induce charges directly affect the three detector signals Q_W, Q_S and Q_Z in Fig. 2. Crosstalk effect exists between the electrodes W, Z and S. The charge division anode consists of a set of isolated electrodes and an approximation method encompassing three irregular-shape electrodes encircled by an enclosing structure is illustrated in Fig. 3(a). Assuming that a charge event covers one of the electrodes, every electrode has been excited differential voltages V_1, V_2 and V_3. Because of the potential difference, the charge Q_{ij} can be induced between the electrodes.

$$Q_{ij} = C_{ij}(V_i - V_j). \tag{6}$$

here C_{ij} is inter-electrode capacitances between the conductor i and the conductor j.

The electrodes of the WSZ anode can be replaced by the capacitance elements and the electrostatically equivalent circuit is shown in Fig. 3(b).

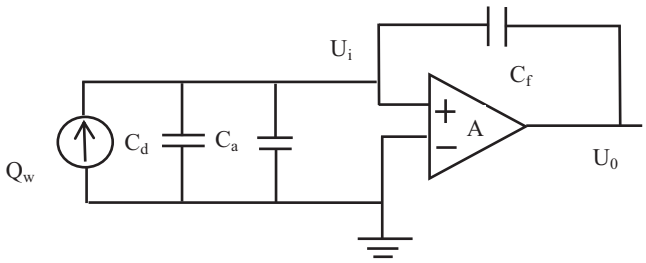

Fig. 2. Charge sensitive amplifier schematic.

If there is no crosstalk effect, the charges should be expressed as

$$Q_i' = C_{ii}\cdot V_i. \tag{7}$$

However, the charge deposited on the electrodes can be expressed using the potential difference as follows,

$$Q_i = Q_i' + \sum_j^N Q_{ij} = C_{ii}V_i + \sum_{j=1}^N C_{ij}(V_i - V_j). \tag{8}$$

C_{ii} is the capacitance between the electrode i to the vacuum chamber. While $\sum_j^N Q_{ij}$ is interpreted as the induced charges. N is the number of electrodes (if anode is the WSZ anode, $N=3$; if anode is the Vernier anode, $N=9$). The expression of charges deposited on the W, S and Z electrode can be written in a matrix, in which $C_{ij}=C_{ji}$,

$$\begin{bmatrix} Q_z \\ Q_w \\ Q_s \end{bmatrix} = \begin{bmatrix} \sum_{j=1}^3 C_{1j} & -C_{12} & -C_{13} \\ -C_{21} & \sum_{j=1}^3 C_{2j} & -C_{23} \\ -C_{31} & -C_{32} & \sum_{j=1}^3 C_{3j} \end{bmatrix} \begin{bmatrix} V_1 \\ V_2 \\ V_3 \end{bmatrix}. \tag{9}$$

Then, V_1, V_2 and V_3 are described as:

$$\begin{bmatrix} V_1 \\ V_2 \\ V_3 \end{bmatrix} = \frac{-1}{\beta}\cdot \begin{bmatrix} b\cdot c - C^2{}_{23} & C_{13}\cdot C_{23} + c\cdot C_{12} & C_{12}\cdot C_{23} + b\cdot C_{13} \\ C_{13}\cdot C_{23} + c\cdot C_{12} & a\cdot c - C^2{}_{13} & C_{12}\cdot C_{13} + a\cdot C_{23} \\ b\cdot C_{13} + C_{12}\cdot C_{23} & a\cdot C_{23} + C_{12}\cdot C_{13} & a\cdot b - C_{12}{}^2 \end{bmatrix} \begin{bmatrix} Q_Z \\ Q_W \\ Q_S \end{bmatrix}. \tag{10}$$

Here $a=\sum_{j=1}^3 C_{1j}$, $b=\sum_{j=1}^3 C_{2j}$, $c=\sum_{j=1}^3 C_{3j}$ and $\beta = c^*C_{12}^2 + b^*C_{13}^2 + a^*C_{23}^2 + 2C_{12}{}^*C_{13}{}^*C_{23}\text{-abc}$.

If the capacitance matrix can be calculated, the proportion of the induced charge deposited on the electrodes which produced by the crosstalk effect of anode can be calculated.

2.4. Distribution of charge cloud footprints

The spatial distribution of charge cloud footprints has been reported in several literatures [5,6], in which the charge footprint distribution spreading over a few pitches can directly influence the image linearity. If the anode pattern is large enough to ensure the charge cloud is within the working area, the image distortion can be eliminated. However, on the one hand, the large area of anode panel can lead to sharply increasing the inter-electrode capacitances, which reduces the detector spatial resolution. On the other hand, the small pitch can increase the numbers of repetitive structure and areas of

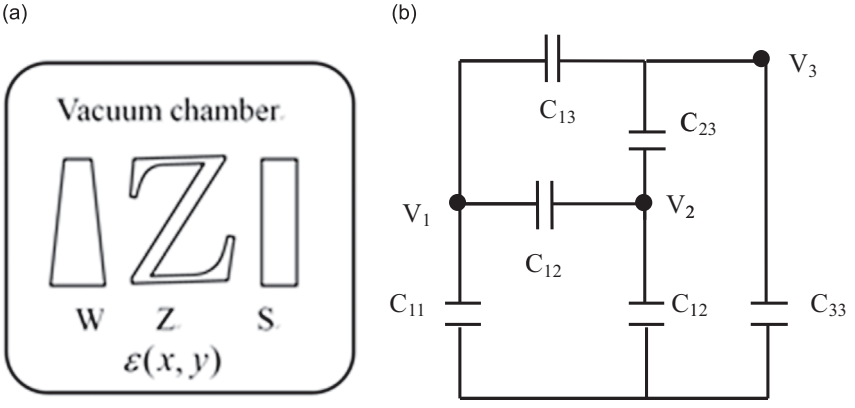

Fig. 3. (a) AWSZ anode involving three conductors signed respectively W, Z and S in vacuum chamber. (b) Electrostatic equivalent circuit of the WSZ anode using lumped capacitances.

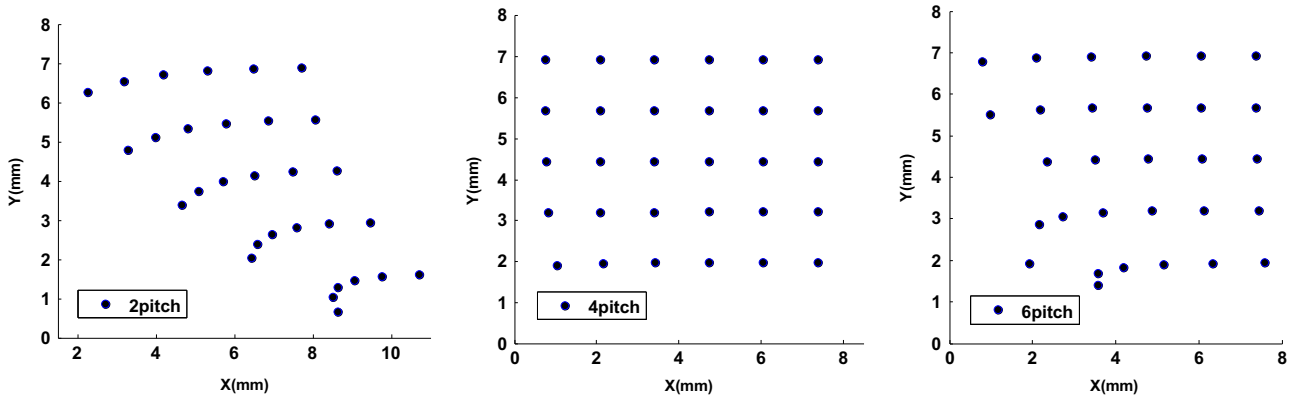

Fig. 4. Simulation images of different charge cloud size.

insulated grooves, which lead to reducing charge deposited on working areas. Moreover, due to the strip electrode varying with width and restricted by the current processing level, the anode pitch can't be designed too small. The WSZ anode pitch is typically around 1–1.5 mm.

Based on the charge cloud emitting from the MCPs approximately obeys Gaussian distribution in Ref [1], the charge cloud model and the WSA anode are established to simulate the detector imaging process and to investigate the imaging linearity in Fig. 4.

Fig. 4 shows that when the charge cloud covers two pitches or six pitches, there are imaging distortions existing and when the charge cloud covers four pitches, the non-linearity of image is basically eliminated. So the distribution of charge cloud should be chosen suitable to eliminate the image modulation according to the requirements of resolution.

In Fig. 1(b), the motion of charge cloud at time t in ref [5] can be described as:

$$r=\sqrt{\frac{2E_e}{m_e}}t\ \sin\ \theta, d=\sqrt{\frac{2E_e}{m_e}}t\ \cos\ \theta+\frac{q_eUt^2}{2m_ed}. \tag{11}$$

where Ee and θ are the electron output energy and angle respectively, d is the distance between MCP and anode, U is the accelerating bias, q_e and m_e are the electron charges and mass.

We can obtain the appropriate size of charge cloud by adjusting the distance d and the gain of MCPs.

3. Simulation technique

3.1. Theory of the WSZ anode detector simulation

Due to the irregular shape of charge division anodes, there is no theoretical formula to calculate the capacitances, the three-dimensional finite element method is introduced to simulate the WSZ anode and to calculate inter-electrode capacitances.

As shown in Fig. 1(a), the anode panel can be regarded as many conductors in the electric field and the physical mechanism of charge division microchannel plate detectors satisfies Maxwell's equations [19].

$$\nabla\times E=-\frac{\partial B}{\partial t}, \tag{12}$$

$$\nabla\times B=\mu J+\mu\varepsilon\frac{\partial E}{\partial t}, \tag{13}$$

$$\nabla\cdot E=\frac{\rho}{\varepsilon}, \tag{14}$$

$$\nabla\cdot B=0. \tag{15}$$

where $\boldsymbol{E}$ represents the electric field, $\boldsymbol{B}$ is the magnetic flux density, $\boldsymbol{J}$ is the free current density, ε is the permittivity, μ is the permeability and ρ is the free charge density. The magnetic flux density $\boldsymbol{B}$ of the detector system is close to 0, so the potential function $\varphi(x,y,z)$ satisfies the following Eq. (2).

$$E=-\nabla\phi(x,y,z) \tag{16}$$

Substituting Eq. (15) into Eq. (13), the potential $\varphi(x,y,z)$ follows the Poisson's Eq. (16). According to the uniqueness theorem [20], if the boundary conditions are given, the unique solution can be obtained. Then the charge Q_i of the conductor i can be achieved by the Gauss's law in Eq. (18),

$$\nabla\cdot\varepsilon\nabla\phi(x,y,z)=\rho. \tag{17}$$

The boundary conditions are given by the following equations:

$$\{\phi(x,y,z)|(x,y,z)\in\tau_i=U\phi(x,y,z)|(x,y,z)\in\tau_s=0, \tag{18}$$

$$Q_i=-\iiint\varepsilon\nabla\phi(x,y,z)\cdot dV. \tag{19}$$

where τ_i is the boundary of the conductive areas in which cloud charge falls, τ_s is the rest areas in which no charge falls.

According to the common definition of capacitance,

$$C_i=\frac{Q_i}{V_i}. \tag{20}$$

The capacitances can be computed by the definition of capacitance (20).

3.2. Simulation process

In the simulation, the modeling software UG and the finite element analysis software (ANSYS) are mainly used.

(1) Filter the graphical interface and select the electric module in ANSYS software.
(2) Modeling. The model of the WSZ anode is built as shown in Fig. 5. According to the existing anode, the design parameters are presented in Table 1.
(3) Define the element type. The solid element3DTet123 is selected as the computing unit and the degrees of freedom are the potential.
(4) Define the material properties. Due to the anode treated in the vacuum chamber, air and silicon glass are applied in the simulation, of which the relative permittivity is $\varepsilon_{air}=1$ and $\varepsilon_{silicon}=2.4$, respectively.
(5) Meshing. The grid of the WSZ anode is shown in Fig. 6(a). The areas of W, S, Z electrodes and insulated grooves are

respectively divided into 10 μm, 10 μm, 10 μm and 5 μm element size. Fig. 6(b) is the mesh dissection diagram of the air range and the division method of Sweep is adopted.

(6) Set the boundary conditions. The outer circle is set as the far field region and the inner circle is the air range.

(7) Enter the solution procedure. The command "CMATRIX" can calculate the inter-capacitances.

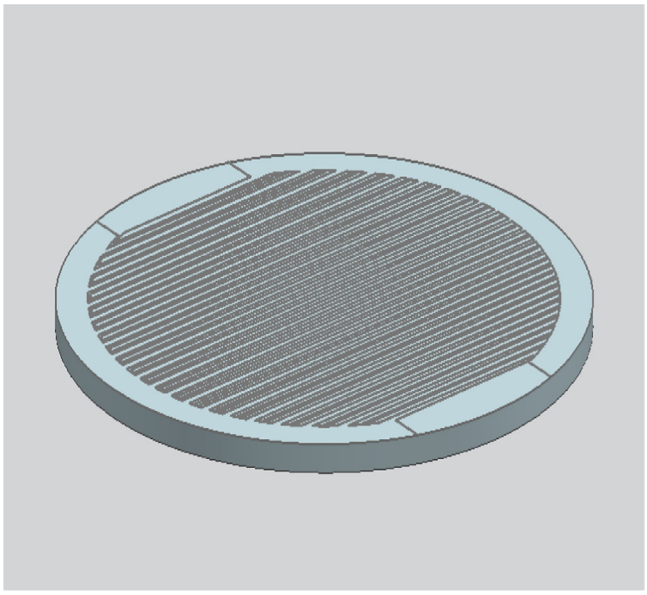

Fig. 5. Model of the WSZ anode built in UG software.

Table 1
Parameters of the WSZ anode model.

Pitch	1.5 mm
The number of pattern pitches	20
Width of insulation channel	70 μm
Substrate thickness	1.2 mm
Anode panel radius	19.8 mm

4. Experimental details

Recently, the charge division anode is manufactured by the picosecond laser machining device [21] as shown in Fig. 7(a). The laser pulse goes through the optical transmission system and reaches the main working area as shown in Fig. 7(b), in which A is the *X* axis platform, B is the *Y* axis platform, C is the *Z* axis platform, D is the galvanometer, E is the focusing mirror, F is the CCD image system, G is the displacement sensor and H is the quartz platform. The levelness of the sample placed on the quartz platform is determined by the CCD image system. The laser path is made by adjusting the scanning galvanometer and the mobile platform.

Fig. 8 shows a WSZ anode developed by us and the parameters are shown in Table 1.The measurements are performed many times by the capacitance meter (Lodestar LVC1500) of which the measurement accuracy is 0.5%.

5. Results and discussion

5.1. Results of simulation and measurement

The main error of simulation U_s are introduced when the WSZ anode model is imported to software.

$$U_S = \left|\frac{\Delta S_W}{S_W}\right| + \left|\frac{\Delta S_Z}{S_Z}\right| + \left|\frac{\Delta S_S}{S_S}\right|. \tag{21}$$

where ΔS_W, ΔS_Z and ΔS_S represent the deformation quantity of the areas of W, S and Z, S_W, S_Z and S_S represent the theoretical value. The overall simulated error is estimated to be of about 3%. Table 2 shows the simulated capacitances and measurement capacitances for the WSZ anode.

The relative norm difference of the results is used and defined as,

$$\text{error} = \frac{|C_M - C_S|}{C_M} \tag{22}$$

where C_M is the measured capacitances and C_S is the simulated capacitances.

Fig. 9 is the relative norm difference of inter-electrode capacitances. Due to ignoring the metal film thickness of the anode (20 μm) and the insulated channel depth by the picoseconds laser

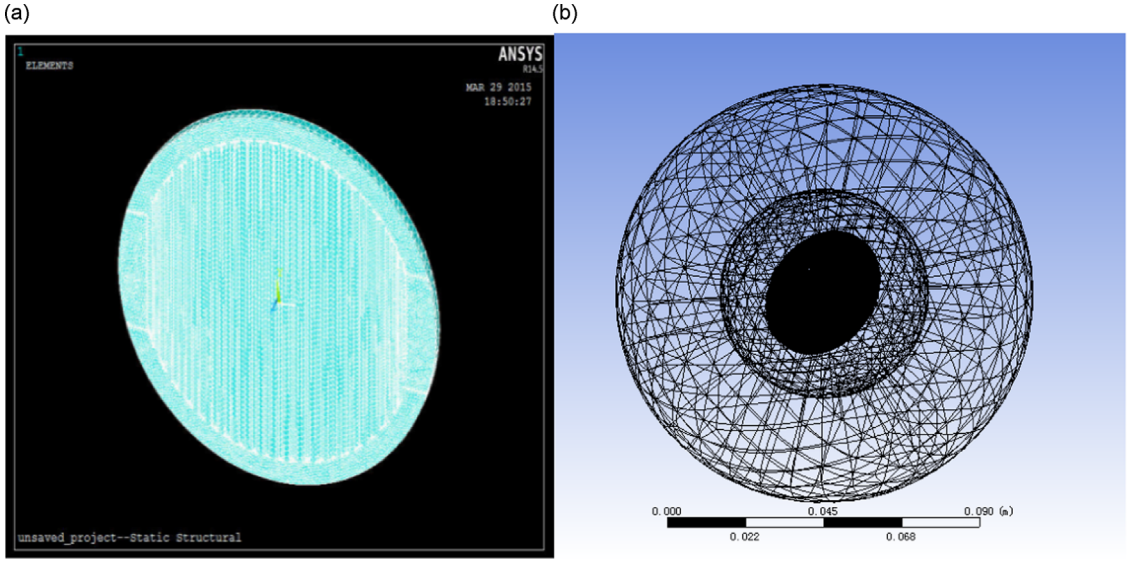

Fig. 6. (a) Mesh dissection diagram of the WSZ anode. (b) Mesh dissection diagram of the air range and far field region.

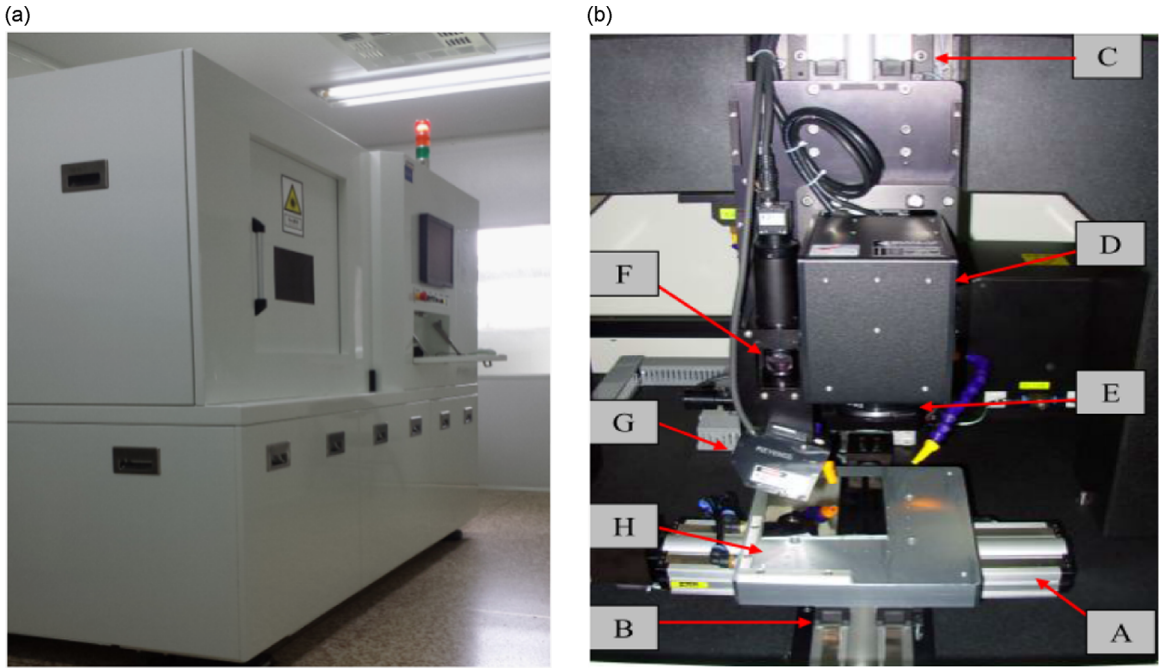

Fig. 7. (a) Picosecond laser micromachining device. (b) Optical components of machining device.

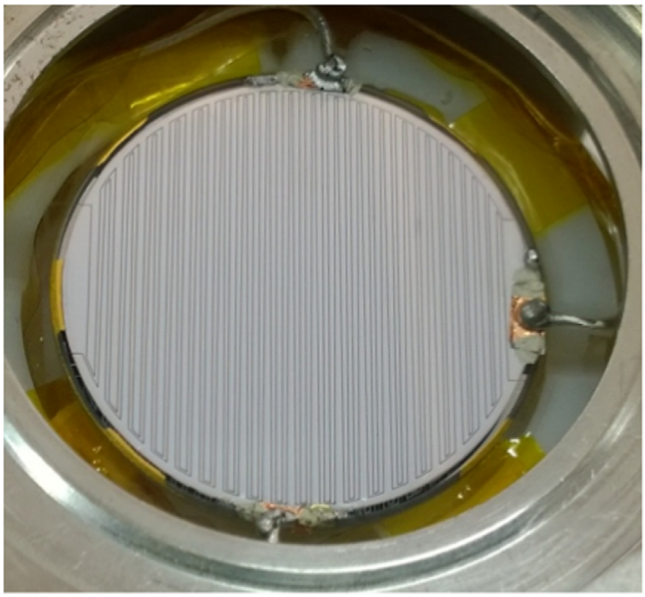

Fig. 8. The fabricated WSZ anode.

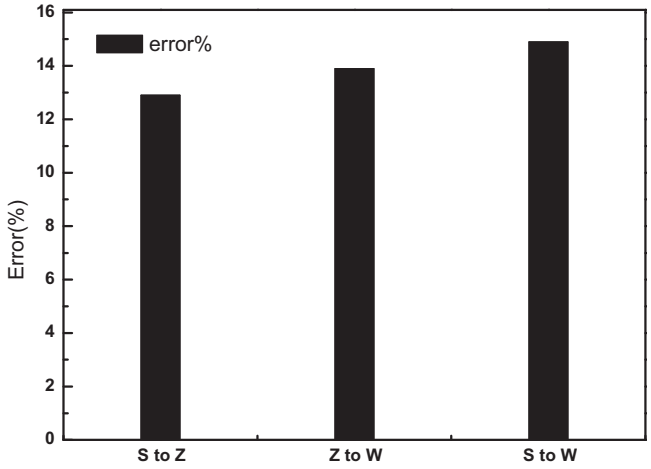

Fig. 9. Relative norm difference of inter-electrode capacitances.

Table 2
Inter-electrode capacitances results of simulation and measurement.

	S to Z	Z to W	S to W
Measured capacitances/pF	44.5 ± 0.5	44.6 ± 0.5	25.7 ± 0.4
Simulated capacitances/ pF	50.25 ± 1.51	50.81 ± 1.52	29.51 ± 1.08

etching (15 μm) which are much less than substrate thickness (1.2 mm), the errors of inter-electrode capacitances are introduced.

5.2. Optimize parameters of the charge division anode

Capacitance values vary with the shape and size of electrodes. Therefore, the inter-electrode capacitances can be varied in some extent when all the anode parameters change. Under satisfying the requirement of processing conditions and the detector imaging performance, the design principle is to make the inter-electrode capacitances as small as possible in order to reduce the induced charges and electronic noise. Before a charge division anode is manufactured, various factors should be taken into account to obtain the best optimization condition.

Recently, the silicon glass ($\varepsilon_{silicon}=2.4$) and printed circuit board ($\varepsilon_{PCB}=4.6$) are normally chosen as the WSZ anode substrate. To investigate the influence of the permittivity on the inter-electrode capacitances, the permittivity ranging from 1.8 to 5.4 is chosen to simulate in Fig. 10. It is obvious that simulated data has a linear relationship with permittivity. The lower substrate permittivity can effectively decrease inter-electrode capacitances.

In addition, the width of insulator channels is an important parameter, which not only affects the inter-electrode capacitances, but also changes areas of the electrodes. As shown in Fig. 11, the inter-electrode capacitances decrease with the width increasing.

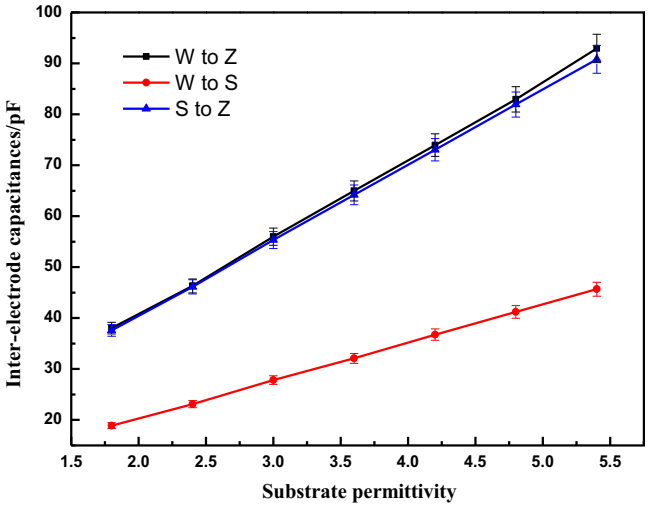

Fig. 10. Inter-electrode capacitances with different permittivity.

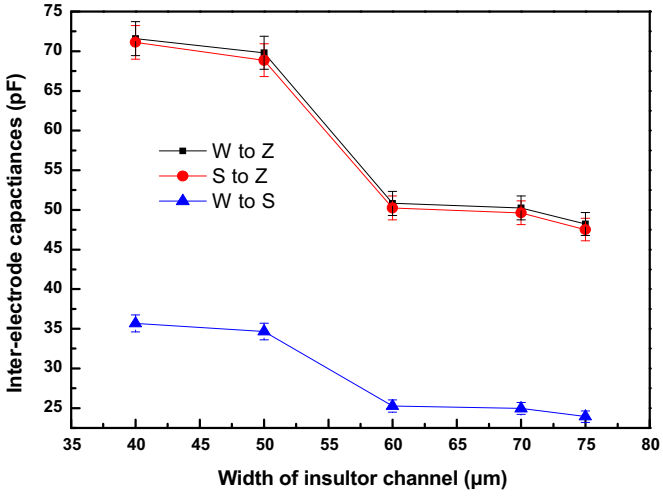

Fig. 11. Inter-electrode capacitances with different width of insulator channels.

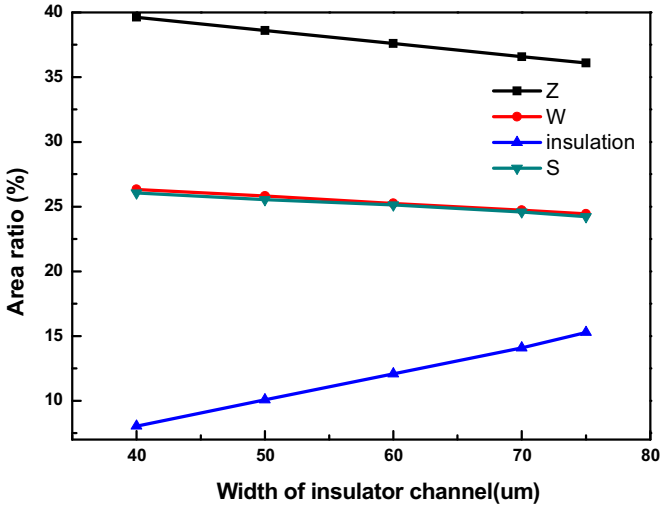

Fig. 12. Area ratios of different width of insulator channels.

However, area ratios of W, S and Z electrodes decrease and area ratio of the insulation channel increase by adjusting the width of the insulator channel in Fig. 12.

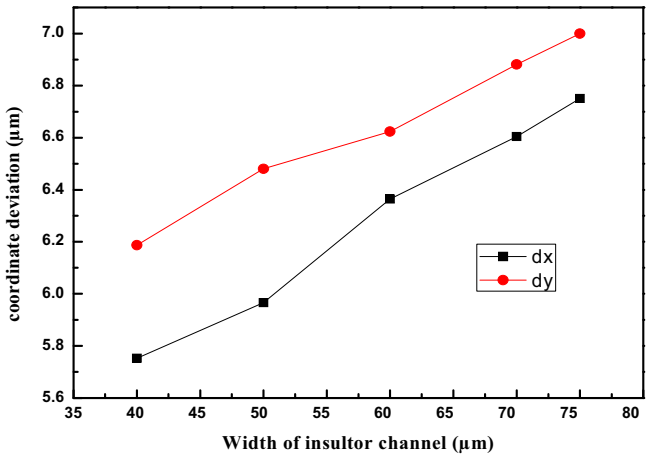

Fig. 13. Coordinate deviation with different width of insulator channel.

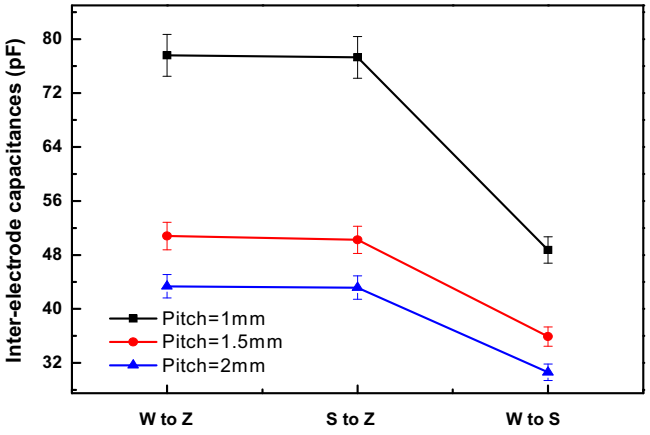

Fig. 14. Inter-electrode capacitances with different sizes of pitch.

The change of the electrode areas influences the effective dynamic range of the WSZ anode which affects imaging linearity. We just consider the influence of electrode area on the collected charge by anode and base on the centroid decoding principle of charge division detectors presented in Ref [10]. The coordinate deviation can be theoretically expressed in Eq. (23).

$$dX = \frac{2L(Q_W+Q_Z)}{(Q_W+Q_S+Q_Z)^2}dQ_S - \frac{2LQ_S}{(Q_W+Q_S+Q_Z)^2}dQ_W - \frac{2LQ_S}{(Q_W+Q_S+Q_Z)^2}dQ_Z$$

$$dY = \frac{2L(Q_S+Q_Z)}{(Q_W+Q_S+Q_Z)^2}dQ_W - \frac{2LQ_W}{(Q_W+Q_S+Q_Z)^2}dQ_S - \frac{2LQ_W}{(Q_W+Q_S+Q_Z)^2}dQ_Z \quad (23)$$

Since the charge ratios are in proportion to the electrode areas ratios, the relationship of the coordinate deviation and width of insulated channel can be seen in Fig. 13. In theory, the wider the insulated channels, the larger the coordinate deviations are.

From Figs. 11 and 13, although the wide insulated grooves make inter-electrode capacitances small, the larger coordinate deviations are introduced. In conclusion, the proper width of insulated channel should be in the range of 55–70 μm by compromising between the imaging linearity and inter-electrode capacitances.

Fig. 14 shows the relationship between inter-electrode capacitances and the different sizes of pitch for the same width of insulated channels and the same areas of anode panel. The size of pitch is not only related to the size of charge cloud, but also affects the spatial resolution. With a fine structure, the resolution of charge division anode detectors can be improved higher.

Therefore, the size of pitch is another parameter which should be seriously taken into account before processing.

The capacitance values decrease with the increasing size of pitch. Although the inter-electrode capacitances having a pitch of 2 mm are lower, the rougher structure can reduce the spatial resolution. Furthermore, although the WSZ anode with a pitch of 1 mm has a fine structure, the inter-electrode capacitances are higher than others, which can introduce much electronic noise and induced charge. For the anode developed by us, we normally design the pitch of 1.5 mm.

6. Conclusions

In conclusion, the three-dimensional WSZ anode model is developed and the finite element method is introduced to calculate the inter-electrode capacitances. The error of the simulated capacitances can be about14%. Based on the comprehensive consideration, the principle of optimizing anode design is to choose lower substrate permittivity, width of insulation channel to be fixed at 55–70 μm and a pitch of 1.5 mm.The study can also be used as a direction to Vernier anodes and have huge potential value in the field of electronic noise for the charge division microchannel plate detectors.

Acknowledgment

The project is supported by the National Natural Science Foundation of China under Grant no.10878004/A03 and the Innovation foundation of the Changchun Institute of Optics, Fine Mechanics and Physics, Chinese Academy of Science No. Y3CX1SS145.

References

[1] O.H.W. Siegmund, M. Lampton, J. Bixler, S. Bowyer, R.F. Malina, IEEE Transaction Nuclear Science 33 (1986) 724.
[2] B.R. Sandel, A.L. Broadfoot, C.C. Curtis, Space Science Review 91 (2000) 197.
[3] M.A. Barstow, N.P. Bannister, R.G. Cruddace, M.P. Kowalski, K.S. Wood, D.J. Yentis, H. Gursky, T.W. Barbee, Proceedings SPIE 4854 (2003) 654–664.
[4] S.W. Dai, Y.Z. Jia, B.M. Zhang, J. Wu, H.X. Xun, E.H. Liu, J.Y. Wei, B. Chen, C.N. Huang, C.B. Xue, J.F. Yang, G.Y. Wang, J.Y. Wang, H.Y. Wang, J.S. An, Science Sin Technol 44 (2014) 361.
[5] A.S. Tremsin, O.H.W. Siegmund, Review Science Instrument 70 (1999) 3282.
[6] J.S. Lapington, Nuclear Instrument and Method A 573 (2007) 247.
[7] J.S. Lapington, B. Sanderson, Proceedings SPIE 4139 (2000) 242.
[8] J.S. Lapington, L.B.C. Worth, Proceedings SPIE 3445 (1998) 546.
[9] J.V. Vallerga, G.C. Kaplan, O.H.W. Siegmund, M. Lampton, R.F. Malina, IEEE Transaction Nuclear Science 36 (1989) 881.
[10] C. Martin, P. Jelinsky, M. Lampton, R.F. Malina, H.O. Anger, Review Science Instrument 52 (1981) 1067.
[11] Yang Hao, Zhao BaoSheng, Yan QiuRong, Liu YongAn, Hu HuiJun, Science China Physics Mechanics Astronomy 54 (2011) 1943.
[12] J.S. Lapington, H.E. Schwarz, IEEE Transaction Nuclear Science 33 (1986) 288.
[13] J. Thornton, Nuclear Instrument and Method A 264 (1988) 523.
[14] H.E. Schwarz, Nuclear Instrument and Method A 238 (1985) 124.
[15] J. Thornton, Nuclear Instrument and Method A 269 (1988) 226.
[16] J.S. Lapington, Nuclear Instrument and Method A 525 (2004) 361.
[17] O. Jagutzki, J.S. Lapington, B.C.L. Worth, Nuclear Instrument and Method A 477 (2002) 256.
[18] O.H.W. Siegmund, S. Clothier, J. Thornton, IEEE Transaction Nuclear Science NS 30 (1983) 503.
[19] R.K. Wangsness, Electromagnetic Fields, 2nd ed., Wiley, Hoboken, NJ (1979), p. 353.
[20] H.A. Haus, J.R. Melcher, Electromagnetic Fields and Energy, Prentice-Hall, Englewood Cliffs, NJ, 1989 (148–151.220-223).
[21] C. Fohl, D. Breitling, K. Jasper, J. Radtke, F. Dausinger, Proceedings. SPIE 4426 (2002) 104.